Letters in Applied NanoBioScience
Open-Access Journal (ISSN: 2284-6808)

Article
Volume 13, Issue 3, 2024, 122
https://doi.org/10.33263/LIANBS133.122

Eco-Friendly Synthesis of Superparamagnetic Fe_3O_4 Nanoparticles from Hibiscus Rosa-Sinensis Leaf Extract and Their Application in RB-4 Dye Removal

Kirti [1], Suantak Kamsonlian [1,*], Vishnu Agarwal [2], Saurabh Yadav [1], Ankur Gaur [1]

[1] Department of Chemical Engineering, Motilal Nehru National Institute of Technology Allahabad, Prayagraj-211004, India
[2] Department of Biotechnology, Motilal Nehru National Institute of Technology Allahabad, Prayagraj-211004, India
* Correspondence:suantakk@mnnit.ac.in;

Scopus Author ID 55258442200
Received: 24.11.2023; Accepted: 7.01.2024; Published: 26.07.2024

Abstract: In this study, iron-based nanoparticles (HS-Fe-NPs) were synthesized using an extract obtained from Hibiscus rosa-sinensis leaves. These nanoparticles were used to remove reactive blue-4 dye from synthetic water samples. The results indicated that a remarkable removal efficiency of over 99.50 percent was achieved for the reactive blue-4 dye with an initial concentration of 100 mg/L at pH 6.0. SEM, XRD, and FTIR analyses were conducted to understand the removal mechanism better and examine the surface changes of HS-Fe-NPs before and after adsorption. Furthermore, UV-VIS analysis was employed to determine the intermediate and final products of the reactive blue-4 dye, shedding light on the potential pathway. VSM analysis was performed to study the magnetic behavior of the synthesized nanoparticles, revealing their superparamagnetic nature with a saturation magnetization of 80.58 emu/g. The Freundlich model successfully described the sorption isotherm, indicating a favorable result based on the experimental data. The highest adsorption capacity of HS-Fe-NPs for RB-4 dye was determined to be 819.67 mg/g. The experimental results revealed that the pseudo-second-order model provided a more accurate representation of enhanced effectiveness. Furthermore, the ΔG° values were found to be negative at all temperatures, indicating the favorable and spontaneous characteristic of the sorption process.

Keywords: magnetized nanoparticles; hibiscus rosa-sinensis leaves; reactive blue-4 dye; adsorption; equilibrium; rate of reaction.

© 2024 by the authors. This article is an open-access article distributed under the terms and conditions of the Creative Commons Attribution (CC BY) license (https://creativecommons.org/licenses/by/4.0/).

1. Introduction

Improper disposal of industrial effluents into water bodies is a significant source of water pollution, resulting in contamination that is often left untreated. This pollution has detrimental effects on aquatic species and other plants and animals in the vicinity of waterways [1,2]. One major contributor to water contamination is the presence of dyes, organic compounds that provide vibrant and consistent colors to various materials. Dyes have complex aromatic molecular structures that make them resistant to decomposition [3]. They are widely used in pulp and paper, plastics, pharmaceuticals, leather, textiles, and cosmetics. Textile dyeing alone accounts for 17-20% of industrial water pollution, according to the World Health Organization (WHO) [4]. The release of colored wastewater from textile dyeing contains toxic substances, including reactive dyes and azo dyes, which alter the chemical composition of water and increase pH, COD, and BOD levels. These hazardous wastes also pose a threat to the environment and contaminate water resources [5,6]. The colored wastewater, due to its poor

light penetration and limited oxygen utilization, severely impacts the aquatic ecosystem [7]. Anthraquinone dyes, the second-largest group of dyes after azo dyes, are widely employed in both industrial and commercial sectors [8]. Reactive Blue 4 (RB4), one of the commonly used anthraquinone dyes in the textile industry, is not only environmentally toxic but also carcinogenic and mutagenic to living organisms [9]. Hence, removing such dyes from wastewater is crucial before its discharge into the environment. Figure 1 illustrates the structure of the Reactive Blue-4 (RB-4) dye [10].

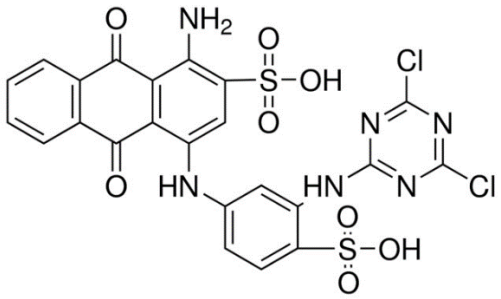

Figure 1. The structure of Reactive blue-4 (RB-4) dye is that the molecular formula is $C_{23}H_{14}Cl_2N_6O_8S_2$, and the molecular weight is 637.43 g/mol.

Various treatment methods for dye removal from contaminated water have been employed, including adsorption, precipitation, photocatalysis, membrane filtration, reverse osmosis, and bioremediation [11]. Nonetheless, these approaches have proven ineffective in eliminating dyes from water effluents due to their pronounced chemical stability, substantial cost, and restricted efficacy. [12-14]. Among these methods, adsorption has gained prominence due to its simplicity, versatility, and effectiveness in removing dyes from contaminated water [15,16]. Nano-adsorbents, with their smaller size and larger surface area, have shown promise in effectively removing dyes [17-20]. Iron-based nanoparticles offer several advantages due to their superparamagnetic properties [21,22]. When subjected to an external magnetic field, these nanoparticles quickly aggregate, facilitating their extraction from aqueous media simply and cost-effectively [23,24]. Superparamagnetic nanoparticles lose their magnetization without a magnetic field and can be readily redispersed.

Consequently, iron-based magnetic nanoparticles have been explored for wastewater purification, providing a more accessible, more affordable, and safer purification process [25-28]. Various synthesis methods, co-precipitation being the most common, can be employed to produce magnetic nanoparticles [29, 30]. The novelty of this research lies in the discovery of eco-friendly materials with potential applications in environmental remediation.

Plant extracts of Hibiscus rosa-sinesis typically contain sugars, terpenoids, polyphenols, alkaloids, phenolic acids, and proteins, which play a role in reducing and stabilizing metal nanoparticles [31-34]. The leaf and flower extracts of this plant have been found to possess various beneficial properties such as antioxidative, anti-cholesterol, anti-hypertensive, blood pressure-regulating, anti-diabetic, chemo-protective, diuretic, antibacterial, anti-tumor, and anticancer effects. [35-38]. So, this study's main focus is producing iron oxide nanoparticles using an extract derived from Hibiscus rosa-sinesis leaves. The synthesis process and characterization of the HS-Fe-NPs are described in detail. The results demonstrate the effectiveness and cost-efficiency of this approach in enhancing dye removal. These particles exhibited superior adsorption efficiency for the RB-4 dye compared

to various other adsorbents. Future research will focus on assessing the efficacy of these nanoparticles in eliminating bacteria and other contaminants present in water.

2. Material and Methods

2.1. Chemicals used.

The chemicals used in this study were analytical grade (AR grade) and used without additional treatment. Deionized water was used to prepare solutions. Glass volumetric flasks and reaction vessels were rinsed with 10% H_2SO_4 and thoroughly washed. Prior to their usage, they were washed multiple times with distilled water. Fresh Hibiscus rosa-sinensis leaves were obtained from a home garden. The chemicals used included ferric sulfate heptahydrate ($Fe_2SO_4.7H_2O$, 99.5%), sodium hydroxide (NaOH, 96 wt.%, pellet form) from Renkem, India, hydrochloric acid (HCL, 37 vol.%), and ethanol (99 vol.%, Merck, Germany) were purchased from Merck India. These chemicals were also high purity (AR grade) and used directly without additional purification. Reactive blue-4 dye RB-4, Sigma-Aldrich, purity ≥ 35 wt. %).

2.2. Synthesis process of HS-Fe-NPs.

Hibiscus rosa-sinensis leaves (HS) were collected and thoroughly rinsed with distilled water to eliminate dust particles from the outer surface, as depicted in Figure 2. An extract was prepared by heating 100 g of freshly chopped and finely ground Hibiscus rosa-sinensis leaves in 500 mL of distilled water at 60°C for 1.5 hours. Once the plant suspension had cooled to room temperature, vacuum filtration was performed, and then the attained product was kept in a freezer at 4°C for future use. The synthesis of nanoparticles was carried out using the co-precipitation method with some modifications as described in [39]. In this process, HS-Fe-NPs were synthesized by adding the leaf extract to a solution of 0.06 M $Fe_2SO_4.7H_2O$ precursor salt mixture with a volume ratio of 2:1, followed by continuous stirring for a duration of 1 hour. The suspension's hue transformed from a light yellow shade to a deep brown color, indicating the reduction of Fe ions.

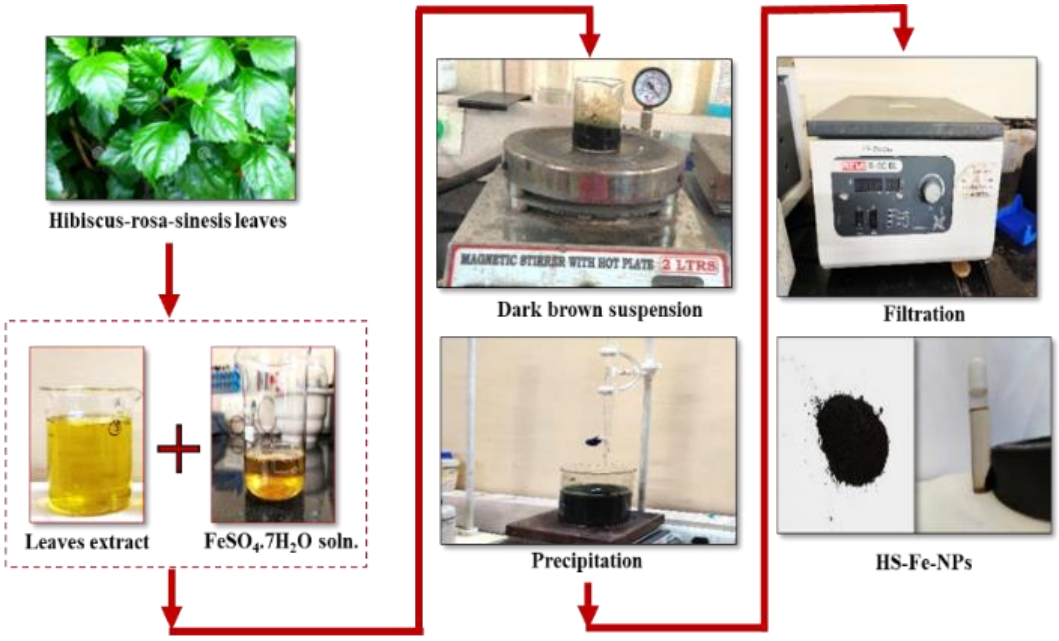

Figure 2. Detailed process of synthesis of nanoparticles from *Hibiscus-rosa-sinesis* leaves.

Precipitation was achieved by the gradual addition of 0.01 M NaOH, followed by the dropwise addition of HCl until a pH of 10.0 was reached. The suspension was left for 30 minutes to allow precipitation. The suspension solution was centrifuged at 5000 rpm for 10 minutes to obtain the nanoparticles. The obtained NPs were thoroughly washed multiple times with deionized water and ethanol, followed by centrifugation until a pH of 7.0 was achieved. Before use, the NPs were vacuum-dried for 24 hours at 40°C and stored in a sample container.

2.3. Adsorbent characterizations.

The plant-based HS-Fe-NPs samples were subjected to a series of analyses serving as adsorbents. Firstly, they were cleaned with acetone, dried, and ground before undergoing ultraviolet light analysis using a Shimadzu double-beam spectrophotometer located at the ChED of MNNIT Allahabad (India). Particle size analysis (PSA) was conducted using the Microtrac\FLEX 11.0.0.4\Databases\MT Database PSA model installed at MNNIT Allahabad, Uttar Pradesh. Prior to SEM analysis, the nanoparticles were coated with gold using a vacuum sputtering device. The surface morphology was then examined using an SEM Zeiss-Evo-50 model Germany made. FTIR analysis was performed using the Perkin Elmer Spectrum Version 10.03.06, USA, to analyze the surface groups and functional characteristics. XRD analysis was performed using an X-ray diffractometer (Rigaku-Smart-Lab-3KW, USA-made). Finally, the magnetic properties and behavior of the synthesized NPs were determined using a VersaLab VSM version 2.0,1.0 VSM (Vibrating Sample Magnetometer) from CIR Lab, MNNIT Allahabad, Uttar Pradesh.

2.4. Batch adsorption experiment.

Batch experiments were conducted where the RB-4 dye concentration was initially set at 100 mg/L. The stock solution was prepared by dissolving 1 gram of RB-4 dye in 1000 mL of distilled water, resulting in a 1000 mg/L concentration. In order to investigate the influence of pH on the adsorption tendency, the pH of the solution was adjusted from 2.0 to 8.0 using a NaOH solution and 0.1 M HCl. The solution was continuously stirred at a rate of 250 rpm over a specified period of time. Subsequently, a strong permanent magnet was employed to extract the adsorbent from the solution, and the remaining concentration of RB-4 dye was determined using a double-beam spectrophotometer. The percentage of RB-4 dye removal was calculated using Equation (1).

$$\%\ Removal = \frac{(C_i - C_e)}{C_i} \times 100 \quad (1)$$

The equilibrium adsorption capacity was determined using Equation (2):

$$q_e = \frac{(C_i - C_e)}{m} \times V \quad (2)$$

where q_e represents the equilibrium amount of solute adsorbed per unit mass of adsorbent, measured in mg/g. C_i denotes the initial concentration of solute in the solution, stated in mg/L. C_e indicates the equilibrium concentration of solute in the solution, also measured in mg/L. The variable m represents the mass of the adsorbent used, expressed in grams, while V signifies the volume of the solution, expressed in L.

The concentration of RB-4 dye in the liquid media was assessed using a Shimadzu double-beam spectrophotometer after every adsorption experiment. In order to understand the adsorption characteristics, various isotherm models such as Langmuir, Temkin, and Freundlich

were employed to analyze the experimental data. Furthermore, kinetic parameters were examined to investigate the adsorption process further.

3. Results and Discussions

3.1. Adsorbent characterizations.

3.1.1. UV-visible spectroscopy.

Figure 3 displays the UV-Vis absorbance spectra of an aqueous extract of Hibiscus rosa-sinesis leaves, $FeSO_4$ * $7H_2O$, and HS-Fe-NPs. The leaf extract of Hibiscus rosa-sinesis exhibits strong absorption bands at 242 nm and 305 nm, which are attributed to the presence of flavonoids, alkaloids, terpenoids, tannins, carbohydrates, and phenolic acids in the extract [40-42]. In the case of magnetic nanoparticles, the UV absorption spectra range from 200 nm to 450 nm, primarily due to the magnetic nanoparticles' absorption and scattering of light, which aligns with previous literature [43,44]. Two absorption peaks are observed at 261 nm and 351 nm wavelengths in the image. These peaks correspond to the reported optimal wavelengths for synthesizing iron-based nanoparticles [4]. The findings of this study are also consistent with the experiments conducted by Devatha *et al*. 2016 [45].

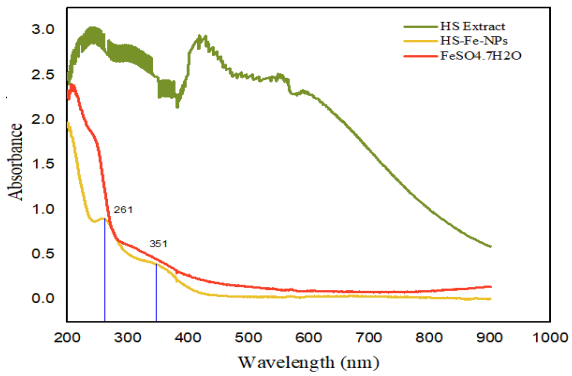

Figure 3. UV–Vis absorption spectrum of a Hibiscus rosa-sinesis leaf extract, $FeSO_4.7H_2O$ salt solution, and HS-Fe-NPs.

3.1.2. Particle size analysis (PSA).

The particle size distribution of the synthesized HS-Fe-NPs was determined using particle size analysis (PSA), and the corresponding differential intensity is presented in Figure 4. The analysis revealed that the particles exhibited a 20-40 nm nano-size range. These findings are consistent with previous studies reported in the literature [46].

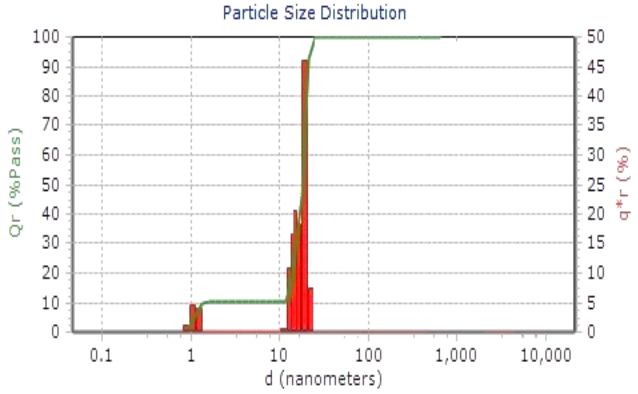

Figure 4. Particle size analysis of synthesized nanoparticles.

3.1.3. Surface morphology.

The surface morphology and texture of HS-Fe-NPs were examined using scanning electron microscopy (SEM) at various magnification levels. In order to facilitate imaging, a layer of gold was applied to coat the NPs. The SEM images in Figure 5(a) revealed that the particles were asymmetrical and smaller than 40 nm in size. Furthermore, SEM analysis was conducted on RB-4 dye-adsorbed Hs-Fe-NPs, and the corresponding results are clearly depicted in Figure 5(b). It can be observed that the physical characteristics of the particles underwent a change upon adsorbing the RB-4 dye. Specifically, the particles exhibited a more spherical shape and increased in size as a consequence of the adsorption process. Similar findings were reported by Prasad *et al*. in 2019 [47].

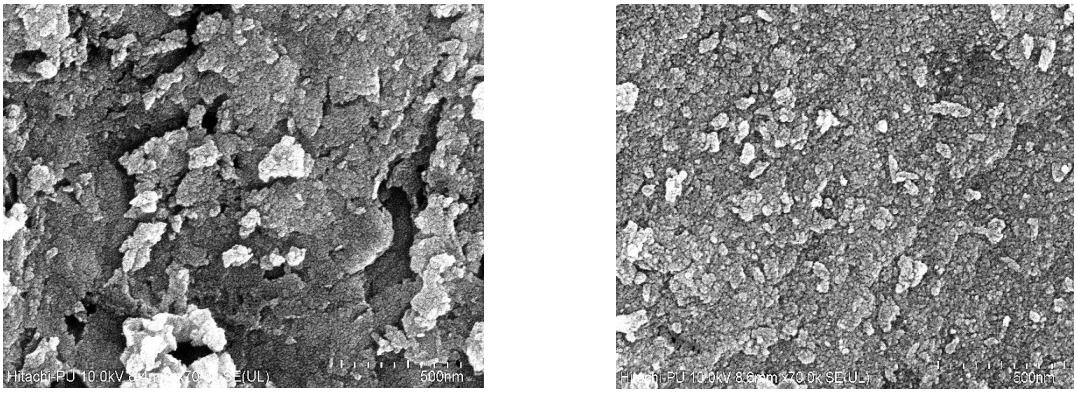

(a) **(b)**

Figure 5. SEM image of **(a)** Raw Hs-Fe-NPs; **(b)** RB-4 dye adsorbed Hs-Fe-NPs.

3.1.4. Fourier transform infrared (FTIR) spectroscopy.

The FTIR technique was employed to analyze the surface groups of the nano-adsorbent and identify the functional groups responsible for RB-4 dye adsorption. The infrared spectrum of the prepared iron nanoparticles was obtained in the range of 400 cm^{-1} to 4000 cm^{-1}, as shown in Figure 6. The presence of phytochemicals involved in the reduction of the precursor metal salt and capping of Fe-NPs was confirmed by the vibrational stretching of the O-H polyphenolic group of Hibiscus rosa-sinensis leaf extract, which exhibited a specific band at 3140.16 cm^{-1} in the range of 3500 cm^{-1} to 3200 cm^{-1} [48].

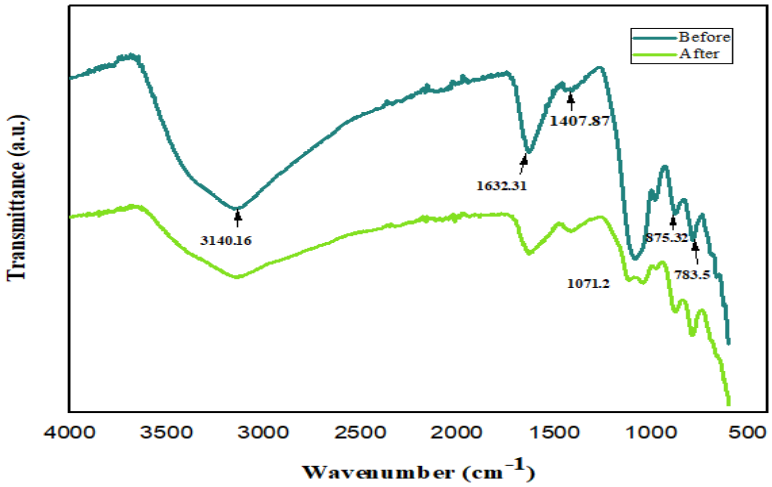

Figure 6. FTIR spectra of HS-Fe-NPs Before and after adsorption of RB-4 dye.

A sharp peak at 1632.31 cm^{-1} was observed, indicating the distortion or elongating vibrations of aromatic ring C=C and -C=O groups [49]. Furthermore, a strong band at 1071.2 cm^{-1} confirmed the presence of a C-O bond. The IR bands at 783.5 cm^{-1} and 463 cm^{-1} corresponded to the stretching and bending vibrations, respectively, of Fe=O in iron oxide [50]. A narrow peak at 1407.87 cm^{-1} was ascribed to NO^{-3} originating from residual nitrate ions [51]. The vibrations of Fe-O bonds in iron oxide were responsible for the adsorption bands at wave numbers below 700 cm^{-1}, indicating the presence of carbon-based groups on the surface of the iron oxide nanoparticles, which prevented their aggregation [52]. The O-H, carboxylate, and aromatic ring groups are expected to be involved in the interactions between RB-4 dye and HS-Fe-NPs, based on previous research on dye adsorbents [53-55].

3.1.5. X-ray diffraction (XRD) analysis.

The X-ray diffraction (XRD) spectrum of iron nanoparticles is presented in Figure 7. The XRD patterns reveal the amorphous and crystalline nature of the HS-Fe-NPs. The characteristic peak of Fe_3O_4 at a 2θ angle of (311) was observed in the synthesized nanoparticles. The presence of magnetite as a distinct phase was confirmed by the intense characteristic peaks at 24.140, 35.790, 54.070, and 64.000 (referenced to ICCD 01-073-9877), corresponding to the (314), (712), (411), and (256) planes, respectively. Additionally, there is a background characteristic between 150 and 250, indicating a partial amorphous character or the presence of phytochemical influences on the HS-Fe-NPs [56]. This is supported by previous studies that have reported the amorphous nature of iron-based nanoparticles synthesized using plant extracts [57,58].

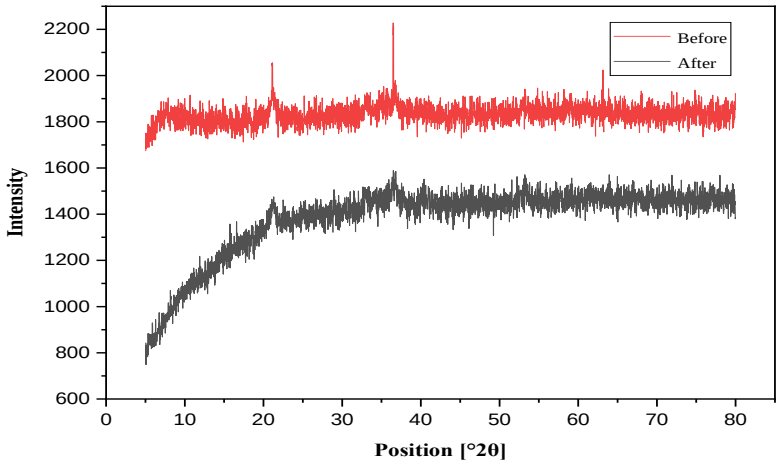

Figure 7. The X-ray diffraction (XRD) spectrum of HS-Fe-NPs for both before and after adsorption of RB-4 dye.

3.1.6. Vibrating sample magnetometer (VSM) analysis.

The magnetic properties of HS-Fe-NPs were evaluated by analyzing the M-H curve using a vibrating sample magnetometer (VSM) at room temperature under a magnetic field range of 6 KOe. The magnetic field strength applied at 298 K was used to determine the magnetic induction of HS-Fe-NPs, as illustrated in Figure 8. The magnetization increased with a rise in the magnetic field. The electromagnetic characteristics of nanoparticles are influenced by various factors, including the synthesis process, magneto-crystalline anisotropy, crystalline spin, and surface properties [59]. The hysteresis curves provided the measurement of the saturation magnetization value for HS-Fe-NPs, which was determined to be 80.58 emu/g. The

samples exhibited minimal hysteresis loop and very low coercivity in their hysteresis curves, suggesting that the nanoparticles possessed superparamagnetic characteristics [60, 61].

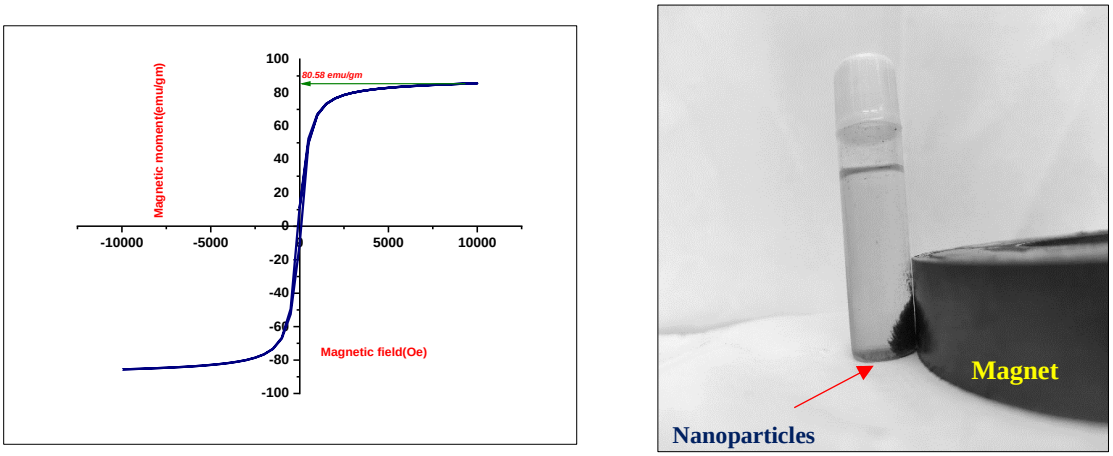

(a) **(b)**

Figure 8. (a) Magnetization curve of HS-Fe-NPs; **(b)** Photography of synthesized nanoparticles attracted towards the magnet.

3.2. Batch adsorption studies.

The effect of pH, adsorbent dose, initial dye concentration, and contact time on the percentage of RB-4 dye removal by HS-Fe-NPs was investigated. The concentration of RB-4 dye in the supernatant was measured at specific time intervals using a spectrophotometer. The spectrophotometer was employed to determine the dye concentration. Figure 9(a) presents actual photographs depicting the RB-4 dye before and after adsorption, while Figure 9(b) illustrates the UV-vis spectra of RB-4 dye prior to and following adsorption, specifically at a wavelength of 595 nm under optimum conditions.

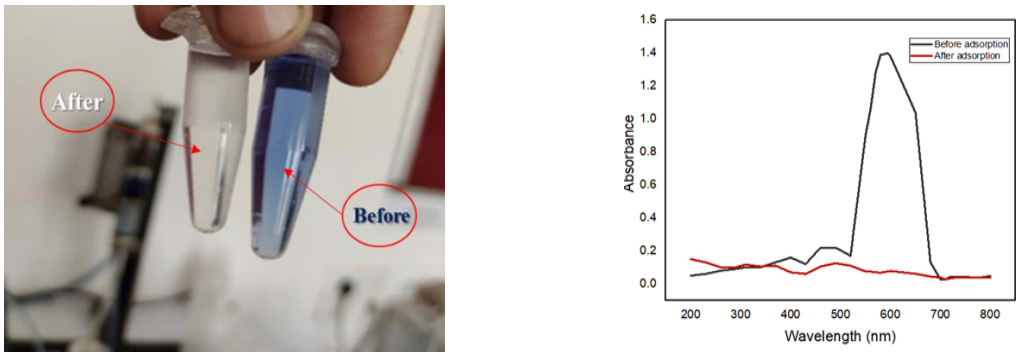

(a) **(b)**

Figure 9. (a) Actual photographic image of RB-4 dye before and after sorption; **(b)** Analysis of UV–vis spectra indicating before and after sorption of RB-4 dye under optimized conditions.

3.3. Effect of pH.

The influence of pH on RB-4 dye removal was examined over a pH range of 2, 4, 6, 8, and 10. The experimental variables were kept constant, including 0.05 g of adsorbent, 100 mL of volume, 100 mg/L of initial dye concentration, 27°C temperature, 150 rpm of agitation, and 960 minutes of run time. Figure 10 (a) illustrates that as the pH increased from 2.0 to 6.0, the percentage of RB-4 elimination increased from 59.2% to 99.4%. Subsequently, as the pH was further increased from 6.0 to 10.0, a decline in the percent removal of RB-4 was observed,

dropping from 99.4% to 81.2%. The highest removal of RB-4 was achieved at pH 6.0 (99.4%). Surprisingly, the removal of RB-4 under strongly acidic conditions (pH 2.0) was lower compared to other pH levels. This outcome could be attributed to the protonation of NH_2 groups in acidic conditions, resulting in enhanced electrostatic interactions between the protonated amine groups of HS-Fe-NPs and the SO_3 groups of RB-4 molecules. On the other hand, the maximum RB-4 removal by the adsorbent decreased to 81.2% as the pH of the dye solution was further increased to pH 10.0. A decrease in dye adsorption capacity may explain this observation due to the deprotonation of NH_2 groups. Consequently, all decolorization experiments were performed at the optimal pH of 6.0. Similar findings regarding the effect of pH on RB-4 removal were reported previously by Satheesh *et al*. 2016 [62].

3.4. Effect of HS-Fe-NPs dosage.

The amount of adsorbent used plays a crucial role in determining the adsorption capacity. In order to examine the impact of HS-Fe-NPs dosage on RB-4 dye degradation, experiments were conducted under the conditions of pH 6.0, a temperature of 27°C, agitation at 180 rpm for 120 minutes, in a 100 mL container, with an initial concentration of RB-4 dye (100 mg/L). The experimental data indicated that increasing the adsorbent dosage from 0.02 to 0.1 g increased RB-4 dye removal from 50.11% to 98.72%, with the highest percentage removal observed at an adsorbent dosage of 0.06 g as shown in Figure 10 (b). However, no further improvement in removal was observed when the adsorbent dosage was increased from 0.06 g to 0.1 g, suggesting that the optimal adsorbent dosage had been reached. The enhancement in dye removal with higher adsorbent dosage can be attributed to the larger effective surface area and increased number of adsorption binding sites provided by the HS-Fe-NPs [63].

3.5. Effect of initial dye concentration.

To investigate the impact of dye concentration on RB-4 dye removal, a series of solutions with concentrations ranging from 100 to 500 mg/L were employed. The experiments were conducted under constant conditions, including a fixed HS-Fe-NPs concentration of 0.06 g, a temperature of 27°C, an agitation speed of 180 rpm, a contact time of 120 minutes, and a pH of 6.0. The results, depicted in Figure 10 (c), indicated that the percentage of dye removal decreased from 99.3% to 50.3% as the initial dye concentration increased. This trend can be attributed to the presence of numerous active sites on the surface of HS-Fe-NPs, which are capable of adsorbing all the dye molecules in low-concentration solutions. However, as the concentration of dye molecules in the solution rose, the accessibility of active sites on HS-Fe-NPs diminished, resulting in a significant decline in the percentage of dye removal with increasing initial dye concentration [64]. Consequently, better removal efficiency was achieved at lower initial dye concentrations but substantially diminished at higher concentrations.

3.6. Effect of contact time.

In order to identify the ideal time period for achieving the highest RB-4 dye removal efficiency by HS-Fe-NPs, the optimal duration was investigated. Batch mode adsorption experiments were conducted for various time intervals ranging from 5 to 240 minutes while keeping other experimental parameters constant, including volume (100 mL), pH (6.0), adsorbent dose (0.06 g), and agitation speed (180 rpm). The results, illustrated in Figure 10 (d),

revealed that 99.04% of the dye was removed when the initial RB-4 dye concentration was 100 mg/L. Initially, there was a rapid increase in dye absorption, which can be attributed to the availability of unoccupied dye adsorption sites. As the active sites on HS-Fe-NPs became saturated with dye molecules, the adsorption process continued at a slower pace [65,66]. However, with the passage of time, the adsorbent's surface became saturated with RB-4 dye molecules, resulting in reduced electrostatic dispersion between the adsorbed dye molecules and those in the aqueous solution. This hindered further adsorption of dye molecules onto the adsorbent. Consequently, the adsorption process diminished over time. Other researchers have reported similar observations [67,68].

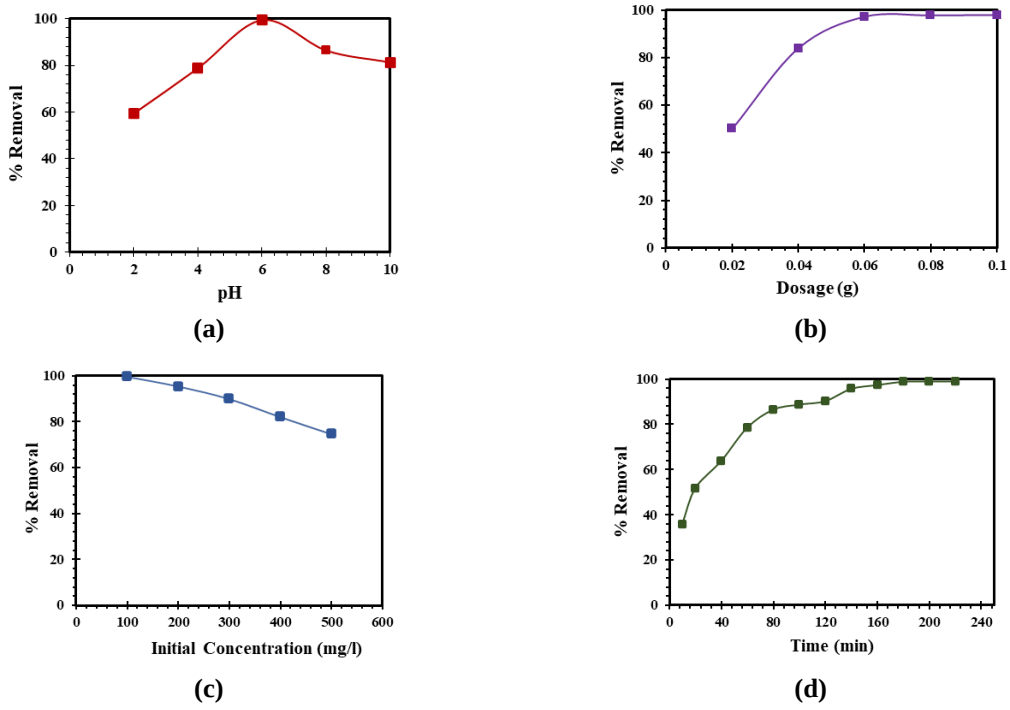

Figure 10. Studied process parameters for adsorption of RB-4 dye onto the surface of Hs-Fe-NPs from aqueous solutions: **(a)** effect of pH; **(b)** effect of adsorbent dosage; **(c)** effect of initial dye concentration; **(d)** effect of contact time.

3.7. Isotherm modeling.

The adsorption experiments were conducted in batch mode using 100 mL of adsorbate solution with an initial concentration of 100 mg/L of RB-4 dye. The purpose was to examine the sorption isotherms of the dye on the synthesized nanoparticles. In order to understand the equilibrium adsorption of the dye on the surface of Hs-Fe-NPs, three adsorption isotherm models, namely Langmuir, Freundlich, and Temkin, were applied to the adsorption data. The Langmuir isotherm model is expressed by Eq. (3).

$$\frac{C_e}{q_e} = \frac{C_e}{q_m} + \frac{1}{K_L q_m} \quad (3)$$

where q_m denotes the RB-4 dye's highest adsorption uptake capacity (mg/g), and K_L denotes the Langmuir constant (L/mg). The separation factor (RL) determines the adsorption process's sustainability. The separation factor can be determined using Eq. (4):

$$R_L = \frac{1}{1+K_L.C_i} \quad (4)$$

The isotherm is called linear in the case of $R_L = 1$, favorable if $0 < R_L < 1$, unfavorable if $R_L > 1$, and irreversible if $R_L = 0$. The adsorption parameters were estimated using the linear

expression derived from graphical plots of $1/q_e$ versus $1/C_e$ (Figure 11 a). Langmuir isotherm parameters and correlation coefficient for RB-4 dye are given in Table 1.

The model for Freundlich isotherm is given in Eq. (5):

$$logq_e = \left(\frac{1}{n}\right) logC_e + logK_F \quad (5)$$

where the degree of adsorbent surface heterogeneity is denoted by n, while K_F represents the Freundlich constant (mg/g). In a favorable adsorptions scenario, (1/n) is expected to be less than 1. The values of the Freundlich parameters were obtained by plotting log q_e against log C_e (Figure 11 b). Table 1 presents the estimated parameters of the Freundlich isotherm.

Also, the Temkin isotherm model is represented in Eq. (6):

$$q_e = \left(\frac{RT}{b_T}\right) lnA_T + \left(\frac{RT}{b_T}\right) lnC_e \quad (6)$$

where the gas constant, represented as R and valued at 8.314 J $mol^{-1}K^{-1}$, is a constant associated with gases. The Temkin constant, denoted as b_T and measured in J/mol, signifies the heat of adsorption. The absolute temperature is indicated as T and measured in Kelvin. The equilibrium binding constant, denoted as A_T with units of L/g, represents the value at which equilibrium is attained. The estimation of Temkin parameters was conducted by plotting q_e v/s ln C_e, as shown in Figure 11(c). The values of Temkin parameters for RB-4 dye are provided in Table 1.

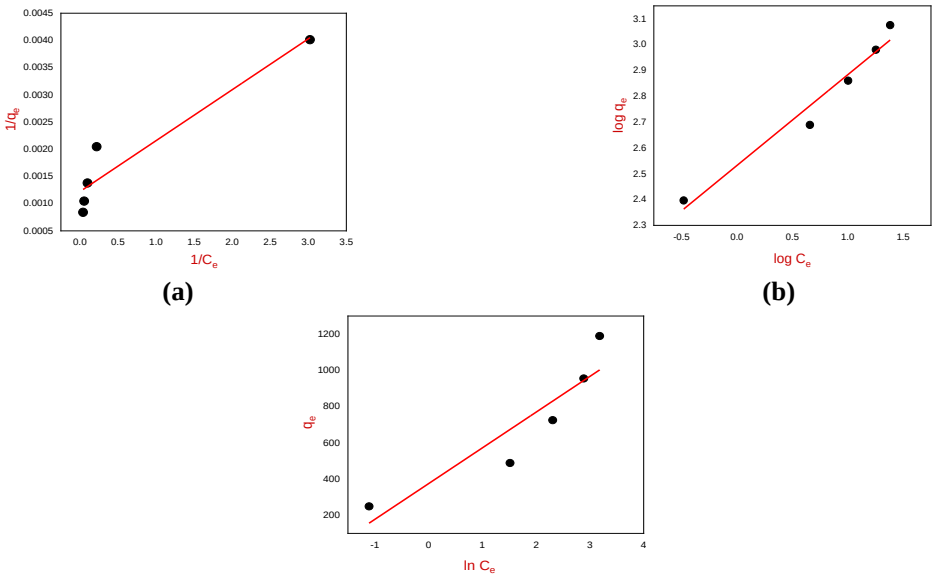

Figure 11. Isotherm studies for adsorption of RB-4 dye onto the surface of Hs-Fe-NPs from aqueous solutions: **(a)** Langmuir isotherm; **(b)** Freundlich Isotherm; **(c)** Temkin isotherm.

Table 1. The adsorption of RB-4 dye on Hs-Fe-NPs can be explained using an adsorption isotherm model, which is characterized by various adsorption parameters.

	Langmuir Isotherm			**Freundlich Isotherm**			**Temkin Isotherm**		
Parameter	q_m *(mg/g)*	K_L *(L/mg)*	R^2	K_F *(mg/g(L/mg)$^{1/n}$)*	*(1/n)*	R^2	A_T *(L/mg)*	b_T *(kJ/mol)*	R^2
Value	909.09	1.30	0.90	340.44	0.35	0.96	6.68	197.30	0.78

The RB-4 dye adsorption was accurately represented by the Freundlich isotherm model, indicating a multilayer distribution onto adsorption sites [10]. The value of 1/n is utilized to categorize an isotherm as irreversible (1/n = 0), favorable (0 > 1/n < 1), or unfavorable (1/n > 1). In the case of the Freundlich isotherm, the 1/n value of 0.35 suggests a favorable adsorption

behavior. Furthermore, the Langmuir model yielded a q_{max} value of 819.67 mg/g at 28°C. This result establishes HS-Fe-NPs as an excellent adsorbent for dye removal, owing to its high adsorption capacities and straightforward process compared to typical activated carbon adsorbents. Shradhha *et al*. (2021) also obtained similar results, obtaining 138.89 mg/g, and the Freundlich isotherm model indicated a good fit for the equilibrium [29]. Table 2 compares HS-Fe-NPs' performance in dye elimination with other iron-based nanoparticles as adsorbents, underscoring the potential of HS-Fe-NPs as an alternative adsorbent for removing dyes from aqueous environments.

Table 2. Literature review on different types of adsorbents utilized for the elimination of dyes.

Type of dye	Adsorbents	q_{max} (mg/g)	Reference
Reactive blue-4	Carbon nanotubes	502.5	[72]
Basic Blue 9	Fe_3O_4 nanoparticles loaded onto wheat straw	627.1	[19]
Methylene blue	Zanthoxylum armatum DC	466.6	[40]
Methylene blue	Attapulgite clay	215.73	[27]
Acid Blue 113	Thunbergia grandiflora leaf	138.89	[29]
Crystal violet	Ferula persica flower	454.5	[30]
Crystal Violet	Fraxinus chinensis Roxb leaf	88.65	[73]
Crystal violet	Grapefruit peel	254.16	[74]
Methylene blue	Immobilized Agrobacterium fabrum biomass, along with iron oxide nanoparticles	91	[50]
Reactive blue-4	*Hibiscus rosa-sinensis* leaf	819.67	Present study

3.8. Kinetic modeling.

In this study, batch mode adsorption was employed to investigate the adsorption kinetics of RB-4 under specific conditions: a pH range of 6.0 ± 0.2, a constant temperature of 25°C, and an initial concentration of 100 mg/L. Samples of the adsorbate were collected at regular intervals, separated, and analyzed to determine the remaining concentration of RB-4. The adsorption kinetics were analyzed using pseudo-first order, pseudo-second order, and intraparticle diffusion models. The pseudo-first-order kinetic model is represented by Eq. (7).

$$\ln(q_e - q_t) = lnq_e - k_1 t \quad (7)$$

The pseudo-second-order kinetic model is represented by Eq. (8).

$$\frac{t}{q_t} = \frac{1}{k_2 q_e^2} + \frac{t}{q_e} \quad (8)$$

where q_e is the amount of adsorbate adsorbed at equilibrium (mg/g), q_t is the amount of adsorbate adsorbed at time t (mg/g), k_1 *(min^{-1})* and k_2 *(g(mg min)$^{-}$)^{1}* are pseudo-first-order and second-order rate constants respectively and t is the contact time (min).

The intraparticle diffusion model is presented in Eq. (9).

$$q_t = K_{id} t^{1/2} + C \quad (9)$$

where K_{id} denotes the intraparticle rate constant (*mg/g.min$^{1/2}$*), and C represents the thickness of the adsorbate film established on the adsorbent surface during intraparticle diffusion, as determined by measurement (mg/g).

The parameters of the kinetic model are presented in Table 3. Linear regression analysis was performed on the experimental data to calculate these parameters based on the linear form of the kinetic models. By plotting *ln (q_e-q_t)* against t for the pseudo-first-order model and t/q_t against t for the pseudo-second-order model, the values of K_1 and q_e could be determined. Figure 12(a) illustrates the plot for pseudo-first-order RB-4 decolorization, while Figure 12(b) depicts the plot for pseudo-second-order RB-4 decolorization. The intercept and slope of the

curves in Figure 12(c), which represent the plot between q_t and $t^{1/2}$, were used to determine the values of k_{id} and C, respectively. According to the concept of intraparticle diffusion, the transportation of dye molecules from the solution to the pores of HS-Fe-NPs occurs through boundary layers [69]. The results show that the pseudo-second-order equation was best suited for the adsorption data; similar results were also obtained by Fatemeh *et al*., 2016 [16]. The thickness of the boundary layer, indicated by the value of C, varied at different dye concentrations, as detailed in Table 3.

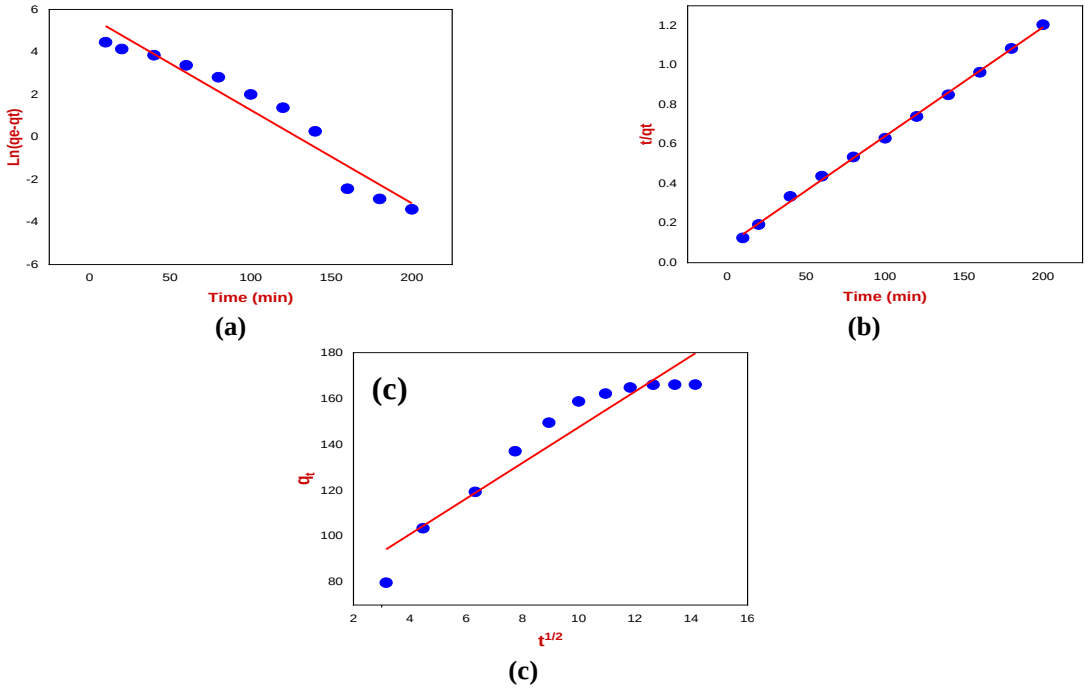

Figure 12. Kinetic models for the adsorption of RB-4 dye onto the surface of Hs-Fe-NPs from aqueous solutions: **(a)** Pseudo first order; **(b)** Pseudo second order; **(c)** Intraparticle diffusion.

Table 3. Estimated kinetic model parameters for RB-4 dye adsorption.

	Pseudo first order			**Pseudo second order**			**Intraparticle diffusion**		
Parameter	q_e *(mg/g)*	k_1 *(min^{-1})*	R^2	q_e *(mg/g)*	k_2 *(g/mg.min)*	R^2	K_{id} *($mg/(g.min)^{1/2}$)*	*C (mg/g)*	R^2
Value	286.51	0.002	0.96	340.43	0.35	0.99	6.679	197.33	0.90

3.9. Adsorption thermodynamics.

Thermodynamic properties, including the change in Gibbs free energy, enthalpy, and entropy, are useful for explaining adsorption characteristics. The nature of adsorption can be elucidated by considering thermodynamic factors such as the change in Gibbs free energy, enthalpy, and entropy. These parameters have been determined using the relationships specified in Eqs. 10, 11, and 12.

$$\Delta G° = -RTlnK_c \quad (10)$$

$$K_c = \frac{q_e}{C_e} \quad (11)$$

$$lnK_c = \frac{\Delta S}{R} + \frac{\Delta H}{RT} \quad (12)$$

where R denotes the gas constant (8.314 J mol^{-1} K^{-1}), K_c signifies the equilibrium constant, and T represents the absolute temperature measured in Kelvin (K). The intercept and slope values obtained from plotting ln K_c against ($1/T$) have been utilized to determine the values of ΔH (enthalpy change) and ΔS (entropy change).

Table 4 presents the thermodynamic parameters (ΔG°, ΔH, and ΔS) at different temperatures, such as 298 K, 303 K, 308 K, and 313 K, respectively. Gibbs free energy change (ΔG°) determines the spontaneity of adsorption. Sorption is thermodynamically favorable and spontaneous when the value of ΔG° is negative across all tested temperatures. The negative ΔG° values across all temperatures indicate that sorption was achievable and spontaneous. Based on Table 4, the adsorption of RB-4 dye using HS-Fe-NPs was viable and spontaneous across all tested temperatures. Moreover, these values increased with higher temperatures, indicating that the adsorption of RB-4 dye was preferable at room temperature. The negative ΔH value, as observed in Table 4, suggests that the adsorption process for RB-4 dye on HS-Fe-NPs is of a physical nature and exothermic in character. Consequently, a higher adsorption capacity was achieved at lower temperatures. Positive ΔS values indicate an increase in system randomness due to the adsorption of RB-4 dye onto the active sites of the HS-Fe-NPs surface. These active sites were considered less organized than the adsorbate (bulk) solution, signifying the favorable selectivity of the adsorbent for RB-4 dye.

Table 4. Estimated thermodynamic parameters for RB-4 dye adsorption.

Dye	ΔH (kJ/mol)	ΔS (J/mol.K)	ΔG° (kJ/mol) at different temperatures (K)				
RB-4	-1.52	4.10	298	303	308	313	318
			-12.10	-12.20	-12.30	-12.40	-12.30

3.10. Mechanism of adsorption.

Figure 13 presents a proposed reaction pathway for the adsorption of RB-4 dye on HS-Fe-NPs. When the green HS-Fe-NPs are introduced into the RB-4 dye solution, they break their chelate bonds with the polyphenolic components and rapidly transform into zero-valent iron. Subsequently, the zero-valent iron undergoes oxidation, generating ferrous ions, which are further oxidized to ferric ions. Throughout the oxidation process, a significant number of electrons are released. In the presence of water, ferric ions produce hydronium (H^+) ions and ferric hydroxide [70]. The released electrons are received by the dye molecules, causing the degradation of the RB-4 dye and the formation of intermediate products [71]. The ongoing reaction between free iron, water, and dissolved oxygen produces hydrogen peroxide. Hydrogen peroxide and dissolved oxygen in the solution react with electrons in the presence of H^+ ions. The catalysis of hydrogen peroxide by ferrous ions generates hydroxyl radicals, which subsequently react with RB-4 dye components. The adsorption mechanism heavily relies on the electrostatic attraction between the positively charged surfaces of HS-Fe-NPs adsorbent and the negatively charged dyes [72]. Moreover, the physical adsorption of metabolites and dye molecules may involve the conversion of ferrous and ferric ions into ferric hydroxides.

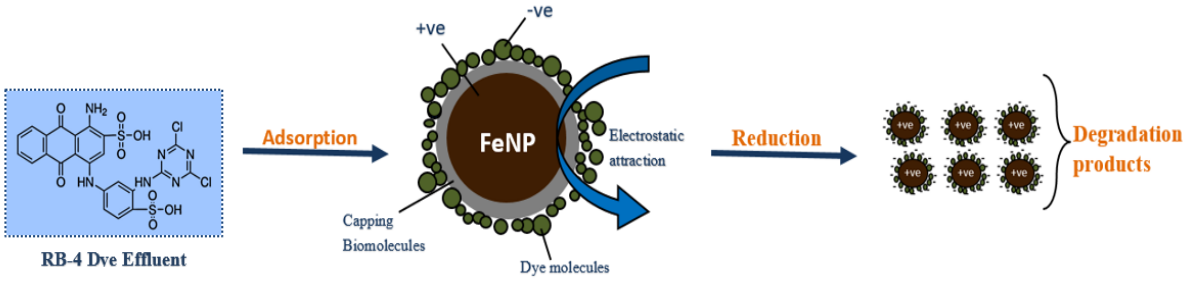

Figure 13. The mechanism for the adsorption of RB-4 dye onto the surface of HS-Fe-NPs.

4. Conclusions and future scope

The primary focus of this study was to produce iron oxide nanoparticles by utilizing a solution derived from Hibiscus rosa-sinesis leaves, which were referred to as HS-Fe-NPs. These nanoparticles were subsequently employed to eliminate dye from a solution. The research findings demonstrated the remarkable efficacy of HS-Fe-NPs in adsorbing the RB-4 dye, particularly at a pH of 6.0. The quantity of HS-Fe-NPs utilized directly influenced the extent of dye adsorption due to an increased number of available adsorption sites. Examination of the synthesized nanoparticles through SEM images revealed their irregular shape and size below 40 nm. Additionally, these nanoparticles exhibited superparamagnetic properties, as evidenced by a saturation magnetization value of 80.58 emu/g indicated in the hysteresis curves. The multilayer Freundlich adsorption isotherm proved to be the most suitable model for describing the equilibrium process, while the pseudo-second-order kinetics model accurately represented the adsorption of the RB-4 dye. Moreover, the adsorption process of RB-4 dye on HS-Fe-NPs is characterized by negative ΔH values (-1.52 kJ/mol), indicating that it is physical adsorption and exhibits an exothermic nature. Hence, the HS-Fe-NPs nanoparticles can be regarded as an affordable and effective adsorbent for treating wastewater containing synthetic dyes.

The synthesized adsorbents should be tested for their ability to remove various other wastewater pollutants, such as heavy metals, organic and inorganic impurities, and bacterial loads. Novel adsorbents should be developed from unexplored plants and their components to create nanoparticles for effective dye removal from water. Further investigations should focus on removing dyes from real groundwater samples.

Funding

This research received no external funding.

Acknowledgments

The authors would like to thank the technical support provided by the CIR Lab and Chemical Engineering Department at MNNIT Allahabad, Prayagraj, for their invaluable assistance throughout this research endeavor.

Conflict of interest

The authors declare no conflict of interest.

References

1. Nekouei, F.; Kargarzadeh, H.; Nekouei, S.; Tyagi, I.; Agarwal, S.; Gupta, V.K. Preparation of Nickel hydroxide nanoplates modified activated carbon for Malachite Green removal from solutions: Kinetic, thermodynamic, isotherm and antibacterial studies. *Process Safe. Environ. Prot.* **2016**, *102*, 85-97, https://doi.org/10.1016/j.psep.2016.02.011.
2. Shrabana, S.; Banerjee, A.; Halder, U.; Biswas, R.; Bandopadhyay, R. Degradation of Synthetic Azo Dyes of Textile Industry: a Sustainable Approach Using Microbial Enzymes. *Water Conserv. Sci. Eng.* **2017**, *2*, 121–131, https://doi.org/10.1007/s41101-017-0031-5.
3. Machado, F.M.; Bergmann, C.P.; Lima, E.C.; Royer, B.; de-Souza, F.E.; Jauris, I.M.; Calvete, T.; Fagan, S.B. Adsorption of Reactive Blue 4 dye from water solutions by carbon nanotubes: experiment and theory. *Phys. Chem. Chem. Phys.* **2012**, *14*, 11139–11153, https://doi.org/10.1039/C2CP41475A.

4. Sudha, M.; Saranya, A.; Selvakumar, G.; Sivakumar, N. Microbial degradation of Azo Dyes: A review. *Int. J. Curr. Microbiol. Appl. Sci.* **2014**, *3*, 670–690.
5. Kant, R. Textile dyeing industry an environmental hazard. *Nat. Sci.* **2012**, *4*, 22-26, https://doi.org/10.4236/ns.2012.41004.
6. Forgacs, E.; Cserháti, T.; Oros, G. Removal of synthetic dyes from wastewaters: a review. *Environ. Int.* **2004**, *30*, 953–971, https://doi.org/10.1016/j.envint.2004.02.001.
7. Dabhane, H.; Chatur, S.; Jadhav, G.; Tambade, P.; Medhane, V. Phytogenic synthesis of gold nanoparticles and applications for removal of methylene blue dye: A review. *Environ. Chem. Ecotoxicol.* **2021**, *3*, 160-171, https://doi.org/10.1016/j.enceco.2021.04.002.
8. Becelic-Tomin, M.; Dalmacija, B.; Rajic, L.; Tomasevic, D.; Kerkez, D.; Watson, M.; Prica, M. Degradation of Anthraquinone Dye Reactive Blue 4 in Pyrite Ash Catalyzed Fenton Reaction. *Sci. World J.* **2014**, *2014*, 234654, https://doi.org/10.1155/2014/234654.
9. Binupriya, A.R.; Sathishkumar, M.; Ku, C.S.; Yun, S.-I. Sequestration of Reactive Blue 4 by free and immobilized *Bacillus subtilis* cells and its extracellular polysaccharides. *Colloids Surf. B Biointerfaces* **2010**, *76*, 179–185, https://doi.org/10.1016/j.colsurfb.2009.10.031.
10. Kirti; Suantak, K.; Vishnu, A.; Ankur, G.; Jin-Won, P. Fe-nanoparticles amalgamation using Lagenaria siceraria leaf aqueous extract with focus on dye removal and antibacterial efficacy. *Korean Chem. Eng. Res.* **2023**, 61, 287–295, https://doi.org/10.9713/kcer.2023.61.2.287.
11. Chauhan, A.K.; Kataria, N.; Garg, V.K. Green fabrication of ZnO nanoparticles using *Eucalyptus spp.* leaves extract and their application in wastewater remediation. *Chemosphere* **2020**, *247*, 125803, https://doi.org/10.1016/j.chemosphere.2019.125803.
12. Holkar, C.R.; Jadhav, A.J.; Pinjari, D.V.; Mahamuni, N.M.; Pandit, A.B. A critical review on textile wastewater treatments: Possible approaches. *J. Environ. Manag.* **2016**, *182*, 351-366, https://doi.org/10.1016/j.jenvman.2016.07.090.
13. Tang, L.; Yu, J.; Pang, Y.; Zeng, G.; Deng, Y.; Wang, J.; Ren, X.; Ye, S.; Peng, B.; Feng, H. Sustainable efficient adsorbent: Alkali-acid modified magnetic biochar derived from sewage sludge for aqueous organic contaminant removal. *Chem. Eng. J.* **2018**, *336*, 160-169, https://doi.org/10.1016/j.cej.2017.11.048.
14. Gadekar, M.R.; Ahammed, M.M. Coagulation/flocculation process for dye removal using water treatment residuals: modelling through artificial neural networks. *Desalin. Water Treat.* **2016**, *57*, 26392-26400, https://doi.org/10.1080/19443994.2016.1165150.
15. Tran, H.N.; Nguyen, H.C.; Woo, S.H.; Nguyen, T.V.; Vigneswaran, S.; Hosseini-Bandegharaei, A.; Rinklebe, J.; Kumar Sarmah, A.; Ivanets, A.; Dotto, G.L.; Bui, T.T.; Juang, R.-S.; Chao, H.-P. Removal of various contaminants from water by renewable lignocellulose-derived biosorbents: a comprehensive and critical review. *Crit. Rev. Environ. Sci. Technol.* **2019**, *49*, 2155-2219, https://doi.org/10.1080/10643389.2019.1607442.
16. Hosseini, F.; Sadighian, S.; Hosseini-Monfared, H.; Mahmoodi, N.M. Dye removal and kinetics of adsorption by magnetic chitosan nanoparticles. *Desalin. Water Treat.* **2016**, *57*, 24378-24386, https://doi.org/10.1080/19443994.2016.1143879.
17. Rodrigues, T.S.; da Silva, A.G.M.; Camargo, P.H. Nanocatalysis by noble metal nanoparticles: controlled synthesis for the optimization and understanding of activities. *J. Mater. Chem. A.* **2019**, *7*, 5857-5874, https://doi.org/10.1039/C9TA00074G.
18. Patra, J.K.; Das, G.; Fraceto, L.F.; Campos, E.V.R.; Rodriguez-Torres, M.d.P.; Acosta-Torres, L.S.; Diaz-Torres, L.A.; Grillo, R.; Swamy, M.K.; Sharma, S.; Habtemariam, S.; Shin, H.-S. Nano based drug delivery systems: recent developments and future prospects. *J. Nanobiotechnology* **2018**, *16*, 71, https://doi.org/10.1186/s12951-018-0392-8.
19. Kannan, U.M.; Giribabu, L.; Jammalamadaka, S.N. Demagnetization field driven charge transport in a TiO_2 based dye sensitized solar cell. *Sol. Energy* **2019**, *187*, 281–289, https://doi.org/10.1016/j.solener.2019.05.029.
20. Jain, R.; Sharma, G.; Kumar, S.; Dubey, A.; Gakhar, N.; Ghosh, C. Potential of plant mediated biosynthesis of iron nanoparticles and their application in dye degradation process. *J. Air Waste Manag. Assoc.* **2023**, *73*, 490-501, https://doi.org/10.1080/10962247.2023.2196964.
21. Kumar, S.; Kumar, M.; Singh, A. Synthesis and characterization of iron oxide nanoparticles (Fe_2O_3, Fe_3O_4): a brief review. *Contemp. Phys.* **2021**, *62*, 144-164, https://doi.org/10.1080/00107514.2022.2080910.

22. Jain, A.; Ahmad, F.; Gola, D.; Malik, A.; Chauhan, N.; Dey, P.; Tyagi, P.K. Multi dye degradation and antibacterial potential of Papaya leaf derived silver nanoparticles. *Environ. Nanotechnol. Monit. Manag.* **2020**, *14*, 100337, https://doi.org/10.1016/j.enmm.2020.100337.
23. Gola, D.; kriti, A.; Bhatt, N.; Bajpai, M.; Singh, A.; Arya, A.; Chauhan, N.; Srivastava, S.K.; Tyagi, P.K.; Agrawal, Y. Silver nanoparticles for enhanced dye degradation. *Curr. Res. Green Sustain. Chem.* **2021**, *4*, 100132, https://doi.org/10.1016/j.crgsc.2021.100132.
24. Mosleh-Shirazi, S.; Kasaee, S.R.; Dehghani, F.; Kamyab, H.; Kirpichnikova, I.; Chelliapan, S.; Firuzyar, T.; Akhtari, M.; Amani, A.M. Investigation through the anticancer properties of green synthesized spinel ferrite nanoparticles in present and absent of laser photothermal effect. *Ceram. Int.* **2023**, *49*, 11293-11301, https://doi.org/10.1016/j.ceramint.2022.11.329.
25. Ebrahimian Pirbazari, A.; Saberikhah, E.; Gholami Ahmad Gorabi, N. Fe_3O_4 nanoparticles loaded onto wheat straw: an efficient adsorbent for Basic Blue 9 adsorption from aqueous solution. *Desalin. Water Treat.* **2016**, *57*, 4110-4121, https://doi.org/10.1080/19443994.2014.989918.
26. Peng, L.; Qin, P.; Lei, M.; Zeng, Q.; Song, H.; Yang, J.; Shao, J.; Liao, B.; Gu, J. Modifying Fe_3O_4 nanoparticles with humic acid for removal of Rhodamine B in water. *J. Hazard. Mater.* **2012**, *209-210*, 193–198, https://doi.org/10.1016/j.jhazmat.2012.01.011.
27. Zhou, Q.; Gao, Q.; Luo, W.; Yan, C.; Ji, Z.; Duan, P. One-step synthesis of amino-functionalized attapulgite clay nanoparticles adsorbent by hydrothermal carbonization of chitosan for removal of methylene blue from wastewater. *Colloids Surf. A: Physicochem. Eng. Asp.* **2015**, *470*, 248–257, https://doi.org/10.1016/j.colsurfa.2015.01.092.
28. Kharey, P.; Goel, M.; Husain, Z.; Gupta, R.; Sharma, D.; Manikandan, M.; Palani, I.A.; Gupta, S. Green synthesis of biocompatible superparamagnetic iron oxide-gold composite nanoparticles for magnetic resonance imaging, hyperthermia and photothermal therapeutic applications. *Mater. Chem. Phys.* **2023**, *293*, 126859, https://doi.org/10.1016/j.matchemphys.2022.126859.
29. Pai, S.; Kini, S.M.; Narasimhan, M.K.; Pugazhendhi, A.; Selvaraj, R. Structural characterization and adsorptive ability of green synthesized Fe_3O_4 nanoparticles to remove Acid blue 113 dye. *Surf. Interfaces* **2021**, *23*, 100947, https://doi.org/10.1016/j.surfin.2021.100947.
30. Nasiri, J.; Motamedi, E.; Naghavi, M.R.; Ghafoori, M. Removal of crystal violet from water using *β*-cyclodextrin functionalized biogenic zero-valent iron nanoadsorbents synthesized via aqueous root extracts of *Ferula persica*. *J. Hazard Mater.* **2019**, *367*, 325-338, https://doi.org/10.1016/j.jhazmat.2018.12.079.
31. Taib, S.H.M.; Shameli, K.; Ali, R.R.; Izadiyan, Z.; Tarmizi, Z.I.A.Green Synthesis of Silver Nanoparticles Using Hibiscus sabdariffa Leaves Extract. *J. Res. Nanosci. Nanotechnol.* **2021**, *3*, 76–81, https://doi.org/10.37934/jrnn.3.1.7681.
32. Mundekkad, D.; Alex, A.V. Analysis of structural and biomimetic characteristics of the green-synthesized Fe_3O_4 nanozyme from the fruit peel extract of *Punica granatum*. *Chem. Pap.* **2022**, *76*, 3863–3878, https://doi.org/10.1007/s11696-022-02130-2.
33. Kashi, R.; Bagheri-Mohagheghi, M.M.; Khorshidi, M. Synthesis and study of structural, optical, and antibacterial properties of silver, copper, and iron metallic nanoparticles prepared by green synthesis. *Appl. Nanosci*. **2023**, *13*, 4343–4360, https://doi.org/10.1007/s13204-022-02700-6.
34. Dehghani, F.; Mosleh-Shirazi, S.; Shafiee, M.; Kasaee, S.R.; Amani, A.M. Antiviral and antioxidant properties of green synthesized gold nanoparticles using *Glaucium flavum* leaf extract. *Appl. Nanosci*. **2023**, *13*, 4395–4405, https://doi.org/10.1007/s13204-022-02705-1.
35. Shahwana, T.; Sirriah, S.A.; Nairat, M.; Boyaci, E.; Eroğlu, A.E.; Scott, T.B.; Hallam, K.R. Green synthesis of iron nanoparticles and their application as a Fenton-like catalyst for the degradation of aqueous cationic and anionic dyes. *Chem. Eng. J.* **2011**, *172*, 258–266, https://doi.org/10.1016/j.cej.2011.05.103.
36. Benković, M.; Valinger, D.; Jurina, T.; Gajdoš Kljusurić, J.; Jurinjak Tušek, A. Biocatalysis as a Green Approach for Synthesis of Iron Nanoparticles—Batch and Microflow Process Comparison. *Catalysts* **2023**, *13*, 112, https://doi.org/10.3390/catal13010112.
37. Kiwumulo, H.F.; Muwonge, H.; Ibingira, C.; Lubwama, M.; Kirabira, J.B.; Ssekitoleko, R.T. Green synthesis and characterization of iron-oxide nanoparticles using Moringa oleifera: a potential protocol for use in low and middle income countries. *BMC Res. Notes* **2022**, *15*, 149, https://doi.org/10.1186/s13104-022-06039-7.
38. Khan, S.; Bibi, G.; Dilbar, S.; Iqbal, A.; Ahmad, M.; Ali, A.; Ullah, Z.; Jaremko, M.; Iqbal, J.; Ali, M.; Haq, I.; Ali, I. Biosynthesis and characterization of iron oxide nanoparticles from Mentha spicata and screening its combating potential against Phytophthora infestans. *Front. Plant Sci.* **2022**, *13*, 1001499, https://doi.org/10.3389/fpls.2022.1001499.

39. Alam, F.; Saqib, Q.N.U. Pharmacognostic study and development of quality control parameters for fruit, bark and leaf of Zanthoxylum armatum (Rutaceae). *Anc. Sci. Life* **2015**, *34*, 147-155, https://doi.org/10.4103/0257-7941.157159.
40. Ramesh, A.V.; Rama Devi, D.; Mohan Botsa, S.; Basavaiah, K. Facile green synthesis of Fe_3O_4 nanoparticles using aqueous leaf extract of *Zanthoxylum armatum* DC for efficient adsorption of methylene blue. *J. Asian Ceram. Soc.* **2018**, *6*, 145-155, https://doi.org/10.1080/21870764.2018.1459335.
41. Buarki, F.; AbuHassan, H.; Al Hannan, F.; Henari, F.Z. Green Synthesis of Iron Oxide Nanoparticles Using *Hibiscus rosa sinensis* Flowers and Their Antibacterial Activity. *J. Nanotechnol.* **2022**, *2022*, 5474645, https://doi.org/10.1155/2022/5474645.
42. Akhbari, M.; Hajiaghaee, R.; Ghafarzadegan, R.; Hamedi, S.; Yaghoobi, M. Process optimisation for green synthesis of zero-valent iron nanoparticles using *Mentha piperita*. *IET Nanobiotechnology* **2019**, *13*, 160–169, https://doi.org/10.1049/iet-nbt.2018.5040.
43. Nahari, M.H.; Al Ali, A.; Asiri, A.; Mahnashi, M.H.; Shaikh, I.A.; Shettar, A.K.; Hoskeri, J. Green Synthesis and Characterization of Iron Nanoparticles Synthesized from Aqueous Leaf Extract of *Vitex leucoxylon* and Its Biomedical Applications. *Nanomaterials* **2022**, *12*, 2404, https://doi.org/10.3390/nano12142404.
44. Bensy, A.D.V.; Christobel, G.J.; Muthusamy, K.; Alfarhan, A.; Anantharaman, P. Green synthesis of iron nanoparticles from *Ulva lactuca* and bactericidal activity against enteropathogens *J. King Saud. Univ. Sci.* **2022**, *34*, 101888, https://doi.org/10.1016/j.jksus.2022.101888.
45. Devatha, C.P.; Thalla, A.K.; Katte, S.Y. Green synthesis of iron nanoparticles using different leaf extracts for treatment of domestic waste water. *J. Clean. Prod.* **2016**, *139*, 1425-1435, https://doi.org/10.1016/j.jclepro.2016.09.019.
46. Lohrasbi, S.; Kouhbanani, M.A.J.; Beheshtkhoo, N.; Ghasemi, Y.; Amani, A.M.; Taghizadeh, S. Green Synthesis of Iron Nanoparticles Using *Plantago major* Leaf Extract and Their Application as a Catalyst for the Decolorization of Azo Dye. *BioNanoSci.* **2019**, *9*, 317–322, https://doi.org/10.1007/s12668-019-0596-x.
47. Prasad, A.R.; Garvasis, J.; Oruvil, S.K.; Joseph, A. Bio-inspired green synthesis of zinc oxide nanoparticles using *Abelmoschus esculentus* mucilage and selective degradation of cationic dye pollutants. *J. Phys. Chem. Solids* **2019**, *127*, 265–274, https://doi.org/10.1016/j.jpcs.2019.01.003.
48. Ranjani, V.A.; Rani, G.T; Sowjanya, M.; Preethi, M.; Srinivas, M.; Nikhil, M. Yeast Mediated Synthesis of Iron Oxide Nano Particles: Its Characterization and Evaluation of Antibacterial Activity. *Int. Res. J. Pharm. Med. Sci.* **2022**, *5*, 12–16.
49. Mohamed, A.; Atta, R.R.; Kotp, A.A.; Abo El-Ela, F.I.; Abd El-Raheem, H.; Farghali, A.; Alkhalifah, D.H.M.; Hozzein, W.N.; Mahmoud, R. Green synthesis and characterization of iron oxide nanoparticles for the removal of heavy metals (Cd^{2+} and Ni^{2+}) from aqueous solutions with Antimicrobial Investigation. *Sci. Rep.* **2023**, *13*, 7227, https://doi.org/10.1038/s41598-023-31704-7.
50. Sharma, S.; Hasan, A.; Kumar, N.; Pandey, L.M. Removal of methylene blue dye from aqueous solution using immobilized *Agrobacterium fabrum* biomass along with iron oxide nanoparticles as biosorbent. *Environ. Sci. Pollut. Res* **2018**, *25*, 21605-21615, https://doi.org/10.1007/s11356-018-2280-z.
51. Urnukhsaikhan, E.; Bold, B.-E.; Gunbileg, A.; Sukhbaatar, N.; Mishig-Ochir, T. Antibacterial activity and characteristics of silver nanoparticles biosynthesized from *Carduus crispus*. *Sci. Rep.* **2021**, *11*, 21047, https://doi.org/10.1038/s41598-021-00520-2.
52. Somchaidee, P.; Tedsree, K. Green synthesis of high dispersion and narrow size distribution of zero-valent iron nanoparticles using guava leaf (*Psidium guajava* L) extract. *Adv. Nat. Sci: Nanoscie. Nanotechnol.* **2018**, *9*, 035006, https://doi.org/10.1088/2043-6254/aad5d7.
53. Yang, Q.-H.; Hou, P.-X.; Bai, S.; Wang, M.-Z.; Cheng, H.-M. Adsorption and capillarity of nitrogen in aggregated multi-walled carbon nanotubes. *Chem Phys. Lett.* **2001**, *345*, 18–24, https://doi.org/10.1016/S0009-2614(01)00848-X.
54. Serp, P.; Corrias, M.; Kalck, P. Carbon nanotubes and nanofibers in catalysis. *Appl. Catal. A: Gen.* **2003**, *253*, 337-358, https://doi.org/10.1016/S0926-860X(03)00549-0.
55. Upadhyayula, V.K.K.; Deng, S.; Mitchell, M.C.; Smith, G.B. Application of carbon nanotube technology for removal of contaminants in drinking water: A review. *Sci. Total Environ.* **2009**, *408*, 1-13, https://doi.org/10.1016/j.scitotenv.2009.09.027.
56. Predescu, A.M.; Matei, E.; Berbecaru, A.C.; Pantilimon, C.; Drăgan, C.; Vidu, R.; Predescu, C.; Kuncser, V. Synthesis and characterization of dextran-coated iron oxide nanoparticles. *R. Soc. Open Sci.* **2018**, *5*, 171525, https://doi.org/10.1098/rsos.171525.

57. Kuang, Y.; Wang, Q.; Chen, Z.; Megharaj, M.; Naidu, R. Heterogeneous Fenton-like oxidation of monochlorobenzene using green synthesis of iron nanoparticles. *J. Colloid Interface Sci.* **2013**, *410*, 67-73, https://doi.org/10.1016/j.jcis.2013.08.020.
58. Farahmandjou, M.; Soflaee, F. Synthesis and Characterization of α-Fe_2O_3 Nanoparticles by Simple Co-Precipitation Method. *Phys. Chem. Res.* **2015**, *3*, 191-196, https://doi.org/10.22036/PCR.2015.9193.
59. García-Merino, B.; Bringas, E.; Ortiz, I. Synthesis and applications of surface-modified magnetic nanoparticles: progress and future prospects. *Rev. Chem. Eng.* **2022**, *38*, 821-842, https://doi.org/10.1515/revce-2020-0072.
60. Kumar, B.; Smita, K.; Cumbal, L.; Debut, A. Biogenic synthesis of iron oxide nanoparticles for 2-arylbenzimidazole fabrication. *J. Saudi. Chem. Soc.* **2014**, *18*, 364–369, https://doi.org/10.1016/j.jscs.2014.01.003.
61. Shu, H.-Y.; Chang, M.-C.; Yu, H.-H.; Chen, W.-H. Reduction of an azo dye Acid Black 24 solution using synthesized nanoscale zero valent iron particles. *J. Colloid Interface Sci.* **2007**, *314*, 89–97, https://doi.org/10.1016/j.jcis.2007.04.071.
62. Satheesh, R.; Vignesh, K.; Rajarajan, M.; Suganthi, A.; Sreekantan, S.; Kang, M.; Kwak, B.S. Removal of congo red from water using quercetin modified α-Fe_2O_3 nanoparticles as effective nanoadsorbent. *Mater. Chem. Phys.* **2016**, *180*, 53-65, https://doi.org/10.1016/j.matchemphys.2016.05.029.
63. Mortazavi-Derazkola, S.; Salavati-Niasari, M.; Amiri, O.; Abbasi, A. Fabrication and characterization of Fe_3O_4@SiO_2@TiO_2@Ho nanostructures as a novel and highly efficient photocatalyst for degradation of organic pollution. *J. Energy Chem.* **2017**, *26*, 17-23, https://doi.org/10.1016/j.jechem.2016.10.015.
64. Gautam, R.K.; Gautam, P.K.; Banerjee, S.; Rawat, V.; Soni, S.; Sharma, S.K.; Chattopadhyaya, M.C. Removal of tartrazine by activated carbon biosorbents of *Lantana camara*: Kinetics, equilibrium modeling and spectroscopic analysis. *J. Environ. Chem. Eng.* **2015**, *3*, 79-88, https://doi.org/10.1016/j.jece.2014.11.026.
65. Madan, S.; Shaw, R.; Tiwari, S.; Tiwari, S.K. Adsorption dynamics of Congo red dye removal using ZnO functionalized high silica zeolitic particles. *Appl. Surf. Sci.* **2019**, *487*, 907-917, https://doi.org/10.1016/j.apsusc.2019.04.273.
66. Salleh, M.A.M.; Mahmoud, D.K.; Karim, W.A.W.A; Idris, A. Cationic and anionic dye adsorption by agricultural solid wastes: A comprehensive review. *Desalination* **2011**, *280*, 1-13, https://doi.org/10.1016/j.desal.2011.07.019.
67. Ghaedi, M.; Ansari, A.; Habibi, M.H.; Asghari, A.R. Removal of malachite green from aqueous solution by zinc oxide nanoparticle loaded on activated carbon: Kinetics and isotherm study. *J. Ind. Eng. Chem.* **2014**, *20*, 17-28, https://doi.org/10.1016/j.jiec.2013.04.031.
68. Qadri, S.; Ganoe, A.; Haik, Y. Removal and recovery of acridine orange from solutions by use of magnetic nanoparticles. *J. Hazard. Mater.* **2009**, *169*, 318–323, https://doi.org/10.1016/j.jhazmat.2009.03.103.
69. Gusain, R.; Gupta, K.; Joshi, P.; Khatri, O.P. Adsorptive removal and photocatalytic degradation of organic pollutants using metal oxides and their composites: A comprehensive review. *Adv. Colloid Interface Sci.* **2019**, *272*, 102009, https://doi.org/10.1016/j.cis.2019.102009.
70. Beheshti, H.; Irani, M.; Hosseini, L.; Rahimi, A.; Aliabadi, M. Removal of Cr (VI) from aqueous solutions using chitosan/MWCNT/Fe_3O_4 composite nanofibers-batch and column studies. *Chem. Eng. J.* **2016**, *284*, 557-564, https://doi.org/10.1016/j.cej.2015.08.158.
71. Wang, H.; Zhou, P.; Guo, R.; Wang, Y.; Zhan, H.; Yuan, Y. Synthesis of Rectorite/Fe_3O_4/ZnO Composites and Their Application for the Removal of Methylene Blue Dye. *Catalysts* **2018**, *8*, 107, https://doi.org/10.3390/catal8030107.
72. Kirti; Suantak, K.; Vishnu, A. Review on Synthesis of Plant-Mediated Green Iron Nanoparticles and Their Application for Decolorization of Dyes. *Mater. Today Proc.* **2022**, 78, 99–107, https://doi.org/10.1016/j.matpr.2022.11.308.
73. Ali, I.; Peng, C.; Khan, Z.M.; Sultan, M.; Naz, I. Green Synthesis of Phytogenic Magnetic Nanoparticles and Their Applications in the Adsorptive Removal of Crystal Violet from Aqueous Solution. *Arab. J. Sci. Eng.* **2018**, *43*, 6245–6259, https://doi.org/10.1007/s13369-018-3441-6.
74. Saeed, A.; Sharif, M.; Iqbal, M. Application potential of grapefruit peel as dye sorbent: Kinetics, equilibrium and mechanism of crystal violet adsorption. *J. Hazard. Mater.* **2010**, *179*, 564–572, https://doi.org/10.1016/j.jhazmat.2010.03.041.

75. Tesnim. D.; Hedi, B.A.; Simal-Gandara, J. Sustainable and Green Synthesis of Iron Nanoparticles Supported on Natural Clays via Palm Waste Extract for Catalytic Oxidation of Crocein Orange G Mono Azoic Dye. *ACS Omega* **2023**, *8*, 34364-34376, https://doi.org/10.1021/acsomega.3c01333.